

Effect of Dopant Concentration on Structural, Optical and Magnetic Properties of $\text{Zn}_{1-x}\text{Ni}_x\text{O}$ Nanocomposites

DHARM VEER¹, RAMMEHARSINGH¹ and HARISH KUMAR^{2*}

¹Department of Physics, Ch. Devi Lal University, Sirsa (Haryana) -125 055, India

²Department of Chemistry, Ch. Devi Lal University, Sirsa (Haryana) -125 055, India
harimoudgill@gmail.com

Received 28 January 2018 / Accepted 8 March 2018

Abstract: $\text{Zn}_{1-x}\text{Ni}_x\text{O}$ ($x=0.0, 0.2, 0.4, 0.6$) nanocomposites were synthesized by co-precipitation method and further annealed at 400 °C. Characterization of nanocomposites was carried out by x-ray diffraction (XRD), Fourier transform infra-red spectrometer (FTIR), UV-Visible spectroscopic, vibrating sample magnetometer (VSM) and transmission electron microscope (TEM) techniques. The structural study confirms that nickel (II) ions replace Zn^{2+} ions in the ZnO lattice without changing its Wurtzite structure and secondary phase (NiO) was observed with the increase in nickel concentration ($x \geq 0.4$). The presence of various functional groups and M-M and M-O chemical bonding were confirmed by FTIR. The optical properties of ZnO nanocrystallinities with Ni-doping was investigated by UV-Vis absorption spectra which indicates red shift in the absorption band on Ni- doping. The morphology and structural information were obtained by the TEM images which shows hexagonal nanoparticles with average particle size of 15-50 nm. The change in magnetic behavior of ZnO nanoparticles with varying Ni^{2+} doping concentration was investigated by VSM.

Keywords: Nanocomposites, Spintronics, Magnetic Semiconductors, Transition metals

Introduction

The oxide semiconductors play an important role in the area of photonic and spintronic. In the field of spintronics, it is essential to develop semiconductors with ferromagnetically polarized carriers at or above room temperature (RT) such that the spin as well as charge carriers can be coupled with an external magnetic field to control the operation of spintronic devices. The idea of spinis helpful in designing devices with higher data processing speed, low power consumption, large integration capacity and better stability. The transition metals doped semiconductors have been the focus of numerous research investigations because of their usual optical properties and promising potential for applications in optoelectronic devices^{1,2}. The transition metals (TM= Ni, Cr, Mn, Fe, Co and Cu) doped ZnO is an exceptional diluted magnetic semiconductors (DMSs) in which the degree of freedom corresponding to spin is added to the charge and it is very attractive nanomaterials used in various electrical, optical and magnetic applications and are believed to be ideal semiconductor

materials for spintronics. DMSs are non-magnetic semiconductors in which a fraction of host cations are replaced by magnetic ions^{3,4}.

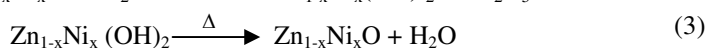
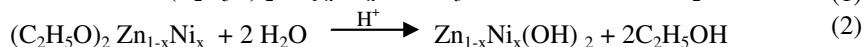
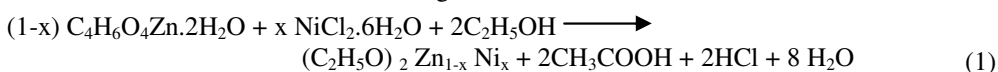
The magnetic semiconductors have attracted major attention of the people working in the area of nanotechnology due to their potential applications in photoelectronics, magnetoelectronics and microwave devices^{5,6}. The room temperature ferromagnetism has been established in various semiconducting matrixes by the dilute doping of transition metals ions⁷ but the synthesis of room temperature ferromagnetism (RTFM) is still a controversial issue. Wakano *et al.*⁸, reported that Ni-doped ZnO nanoparticles exhibits superparamagnetic behavior at room temperature, while Yin *et al.*, observed the paramagnetism in Ni-doped ZnO films⁹. Some authors have observed the RTFM in nanorods, nanowires and films of Ni- doped ZnO film.

Some of the researchers tried to synthesize Ni doped ZnO based DMSs typically in thin films and by different sol-gel reaction routes. Recently, Srinet *et al.*, observed the RTFM in Ni-doped ZnO with low moment by sol-gel route¹⁰. Liu *et al.*, found the RTFM in Ni-doped ZnO thin films prepared by pulsed laser deposition¹¹. Satyarthi *et al.*, claimed the coexistence of intrinsic and extrinsic origins of RTFM in Ni implanted ZnO films¹². In some studies, it is also mentioned that the nature of FM in Ni-doped ZnO does not remain intrinsic upon annealing in various environments at high temperature because of segregation of transition metal ions¹³. Singhla *et al.*¹³, claimed that the ferromagnetism in the hydrogenated and vacuum annealed Ni-doped ZnO disappears upon long reheating at very high temperatures *i.e.*, 700 and 800 °C, respectively. Various chemical methods have been investigated to synthesize the nanoparticles of different material of interest. Most of the ZnO nanocrystals have been synthesized by traditional high temperature solid state methods in which it is very difficult to control the particle properties and also energy consumption. ZnO nanoparticles can be prepared on a large scale at low cost by simple solution based method such as co-precipitation method.

In continuation to our earlier study¹⁴⁻¹⁷, in the present work, we have investigated the structural properties in Ni doped ZnO nanoparticles prepared by co-precipitation method which is simple and low cost method and it yields a good end product and it is less time consuming. The synthesized samples were characterized by various techniques like XRD, FTIR, TEM, UV-Vis absorbance and VSM.

Experimental

AR grade $C_4H_6O_4Zn.2H_2O$, $NiCl_2.2H_2O$, ethanol and trimethylamine were used for synthesis. The stoichiometric amount of zinc acetate dehydrate and nickel chloride were separately kept under constant stirring using a magnetic stirrer to completely dissolve the precursors for 30 minutes. After that the two precursor solutions were mixed with constant stirring for 30 minutes. Trimethylamine solution was added drop by drop slowly for 45 min to the reaction mixture. The solution was continuously stirred at 60 °C for 3.0 h. The white precipitates obtained were filtered and thoroughly washed several times using double distilled water and ethanol to remove the ions possibly remaining in the final product and then dried in an oven at the temperature of 100 °C for 12 hours. After that precipitates were crushed gently to fine powder form with pestle and mortar. Finally, the samples were annealed at 400 °C for 4 h. The following reaction mechanism was followed.



Structural and morphology of the powder samples were determined by x-ray diffraction (XRD) analysis (Panalytical's X'pert Pro using Cu-K α 1, $\lambda = 0.151406$ nm radiations) and transmission electron microscopy (TEM) (Tecnai 200KV Fei Electron Optics $\lambda = 35$ nm). The vibrational frequencies of the bonds in the sample were observed using Fourier transform infrared spectrometer (FTIR) (Perkin Elmer-Spectrum RX-IFTIR) in the wavelength range of 400-4000 cm^{-1} and the optical absorption spectra were recorded at room temperature using UV-Vis spectrometer (Lambda 750 Perkin Elmer) in the wavelength range of 200-800 nm. TGA/DTA studies were carried out by simultaneous thermal analyzer (Perkin Elmer STA 6000, Temperature range 20-995 $^{\circ}\text{C}$). The magnetic study is carried out using VSM (Model PAR 155, Range: 0.00001 to 10000 e.m.u.).

Results and Discussion

In order to study the effect of doping of NiO in the ZnO sample, we have prepared the sample of $\text{Zn}_{1-x}\text{Ni}_x\text{O}$, with $x = 0.0, 0.02, 0.04$ and 0.06 and characterized by XRD, FTIR, UV-Visible, TGA/DTA, TEM and VSM techniques.

XRD Study

Figure 1 shows XRD patterns of $\text{Zn}_{1-x}\text{Ni}_x\text{O}$ ($x = 0.0, 0.02, 0.04$ and 0.06 M) samples annealed at 400 $^{\circ}\text{C}$ and the reflection peaks are indexed to Wurtzite hcp structure of ZnO. The nanostructures shows several peaks of (100), (002), (101), (102), (110), (103), (200), (112), (201), (004) and (202) crystal planes, respectively. All these diffraction peaks were matched well with space group P6 $_3$ mc (No. 186) (JCPDS No. 36-1451). The XRD pattern indicates the formation of hexagonal Wurtzite phase of ZnO and no secondary phase was found for the lower concentration doping samples ($x < 0.04$), which indicates that the Ni ions successfully occupies the lattice site rather than interstitial ones. The occupation of the site of Zn^{2+} in the lattice by the Ni^{2+} ions may induce a crystal defect, resulting from the difference in ion size between zinc and nickel. Therefore, these defects changes stoichiometry of the ZnO lattice. Decrease in the peak intensity and increase in full width at half maxima (FWHM) observed in the XRD patterns of the doped samples confirms a decrease in crystalline quality depending on the Ni content and confirm the incorporation of nickel dopant into the ZnO Wurtzite lattice as a substitute atom. When x reaches 0.04, an additional small diffraction peak correspond to NiO (200) comes into existence at an angle $2\theta \sim 42.5^{\circ}$ for $x = 0.04$ which clearly indicates that phase segregation have occurred in the samples. It is observed that intensity of NiO peak increases sharply and shifts to the lower angle with increasing nickel concentration. This shift corresponds to the strain and replacement of zinc ion by nickel ions. The observed left shift in the NiO diffraction peak from their native place with increasing nickel content is an evident that NiO is distorted to larger spacing where nickel gets oxidized and incorporated into ZnO lattice. Therefore, the saturated solubility¹⁸⁻²¹ of Ni in ZnO is 4.0%. From Bragg's law

$$2d\sin\theta = n\lambda \quad (4)$$

Where, d is lattice spacing, θ is the diffraction angle and λ is the incident wavelength ($\lambda = 0.154056$). The lattice parameters (a and c) of the samples for hexagonal system²² are calculated by using the formula

$$\frac{1}{d^2} = \frac{3}{4} \left(\frac{h^2 + hk + k^2}{a^2} \right) + \frac{l^2}{c^2} \quad (5)$$

Where, h, k, l are miller indices, from Eq. 4 and 5 for $n=1$, we have

$$\sin^2 \theta = \frac{\lambda^2}{4} \left[\frac{4}{3} \left(\frac{h^2 + hk + k^2}{a^2} \right) + \frac{l^2}{c^2} \right] \quad (6)$$

In order to calculate unknowns a and c , the peak in form $(hk0)$ and $(00l)$ should be selected so that a and c are calculated from Eq. 6. On selecting the proper peaks, following expressions are derived for a and c as

$$\alpha = \frac{\lambda \sqrt{h^2 + hk + k^2}}{\sqrt{3} \sin \theta} \quad \text{and} \quad = \frac{\lambda l}{2 \sin \theta} \quad (7)$$

Table 1 shows structural characteristics of $\text{Zn}_{1-x}\text{Ni}_x\text{O}$ nanocomposites. The Ni doping has reduced the size of the lattice parameters a and c which is attributed to the ionic size mismatch between Zn^{2+} (0.074 nm) and Ni^{2+} (0.069 nm). Theoretically, since the ionic radius of Ni^{2+} is smaller than that of Zn^{2+} , the peak (101) of the Ni-doped ZnO should move to larger angle slightly when compared to that of the pure ZnO. From the XRD pattern (Figure 1), it can be seen that the peak (101) of the Ni-doped ZnO slightly shift to higher angle. The shifting of the XRD pattern and corresponding decrease of the lattice parameters suggests that Ni^{2+} ions are successfully incorporated into the ZnO lattice at the Zn^{2+} crystal sites position. The average crystallite size (d) of the nickel doped ZnO powders were estimated from x-ray line broadening using the Debye-Scherrer's equation:

$$d = \frac{0.9\lambda}{\beta \cos \theta} \quad (8)$$

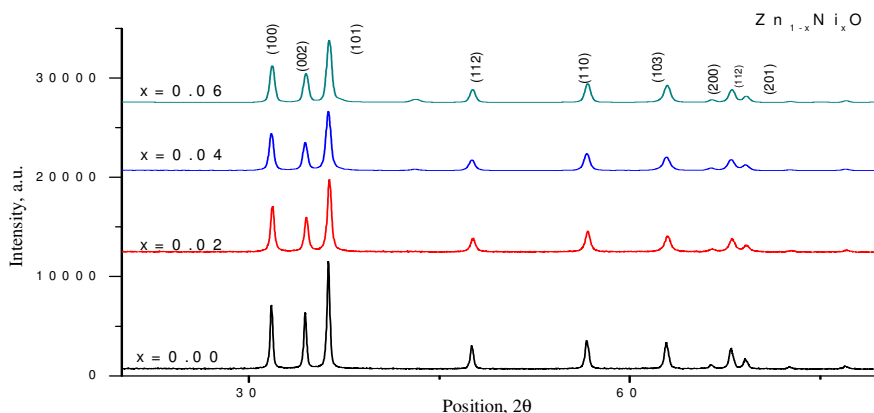


Figure 1. x-Ray diffraction pattern of $\text{Zn}_{1-x}\text{Ni}_x\text{O}$ (for $x=0.0, 0.02, 0.04$ and 0.06) nanocomposites

Table 1. Structural characteristics of $\text{Zn}_{1-x}\text{Ni}_x\text{O}$ nanocomposites

S. No.	Concentration x	Lattice parameter		Strain	Dislocation Density	Average Crystallite Size	
		$a=b$, (Å)	c (Å)			D-S formula	W-H Plot
		$hkl(110)$	$hkl(002)$				
1.	0.00	3.2506	5.2072	0.0036	1.19×10^{-3}	27.86	28.90
2.	0.02	3.2494	5.1920	0.0046	1.68×10^{-3}	22.04	24.34
3.	0.04	3.2448	5.2044	0.0048	2.47×10^{-3}	20.19	20.11
4.	0.06	3.2476	5.1994	0.0058	2.69×10^{-3}	19.02	19.27

The value of dislocation density (δ) was calculated using the relation, $\delta=1/d^2$. The crystallite size of the samples decreases with increasing nickel content which is the result of the surface reaction competition²³. Because the Ni-O bond energy is higher than Zn-O bond energy, the reaction mobility to raise growth surface will decrease with increasing doping concentration.

In Williamson Hall approach, the line broadening due to finite size of coherent scattering region and the internal stress in the prepared sample is also considered. According to Williamson and Hall, the diffraction line broadening is due to crystallite size and strain contribution. However, x-ray peak profile analysis (XPPA) by W-H method is a simplified method which clearly differentiate between size-induced and strain induced peak broadening by considering the peak width as a function of 2θ ²⁴. The W-H method does not follow a $1/\cos\theta$ dependency as in the Scherrer equation but instead varies with $\tan\theta$. This fundamental difference allows for a separation of reflection broadening when both micro and structural cause's small crystallite size and micro strain occur together. The different approaches assume that size and strain broadening are additive component of the total breadth of a Bragg peak. Scherrer equation and $\epsilon=\beta_s/4 \tan\theta$ yield the following equations²⁵.

$$\beta_{hkl} = \beta_D + \beta_s \quad (9)$$

Where, β_D is due to contribution of crystallite size, β_s is due to strain induced broadening and β_{hkl} is the width of the half-maximum intensity of broadening. If we assume that particle size and strain contribution to line broadening are independent of each other and both have a Cauchy-like profile, the observed line width is given by Eq. 9 named as Wilken equation²⁶ as:

$$\beta_{hkl} \cos\theta = \left(\frac{k\lambda}{D} \right) + 4\epsilon \sin\theta \quad (10)$$

The Eq. 10 assumes that the strain is uniform in all crystallographic directions and named as uniform deformation model (UDM). If $\beta_{hkl} \cos\theta$ is plotted as a function of $\sin\theta$ as shown in Figure 2, then from the linear fit of the data, the crystalline size (d) was estimated from the y-intercept and microstrain ϵ from the slope of the linear fit.

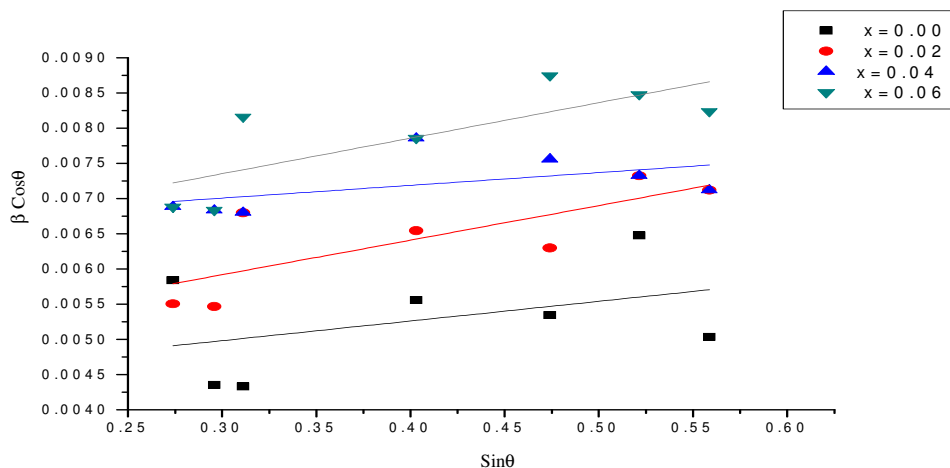


Figure 2. W-H plots of $Zn_{1-x}Ni_xO$ (for $x= 0.0, 0.02, 0.04$ and 0.06) nanocomposites

FTIR Study

Figure 3 shows the FTIR spectra of $\text{Zn}_{1-x}\text{Ni}_x\text{O}$ ($x = 0.0, 0.02, 0.04, 0.06$) nanocrystals annealed at 400°C . From the FTIR spectra, the strong vibrational mode observed at 525 cm^{-1} is assigned to stretching vibration of ZnO^{27} . However, in case of 2.0, 4.0 and 6.0%, Ni doped samples, the value of absorption bands were found to be left shifted at $530, 534$ and 529 cm^{-1} , respectively. The peaks appearing between 500 and 700 cm^{-1} were assigned to the metal oxygen (M-O) stretching mode. The FTIR spectrum in the wave number range $< 1000\text{ cm}^{-1}$ represents the change in the peak position of ZnO absorption bands reflects that Zn-O-Zn network is perturbed by the presence of Ni in its environment. Therefore, FTIR results also indicate that Ni is occupying Zn position in ZnO matrix as observed in XRD patterns. The vibration mode at wave number 701 and 979 cm^{-1} were attributed to the vibrations of Zn-O-Ni local bonds and defect states, respectively and associated with Ni^{2+} occupation at Zn^{2+} sites. Because the ionic radii mismatch between Ni^{2+} and Zn^{2+} , intrinsic host lattice defects are activated. The weak absorption band centered at 1369 cm^{-1} attributed to the stretching vibration of C=O and C=H groups. The transmission band at 1523 and 1417 cm^{-1} is due to the carbonyl groups of the carboxylate ions which might remain adsorbed on the surface of ZnO. The absorption peak at 1620 cm^{-1} corresponds to the bending vibration of the interlayer water molecules²⁸. Absorption peaks observed at around 2342 cm^{-1} are assigned to the CO_2 mode which is due to atmospheric CO_2 and other transmission band at 2928 cm^{-1} is assigned to a residual organic component. The broad absorption band at 3495 cm^{-1} corresponds to the O-H stretching vibrations of water present in ZnO. As the concentration of the dopant is increased then the peaks are shifted to left indicating the incorporation of nickel in the ZnO lattice site.

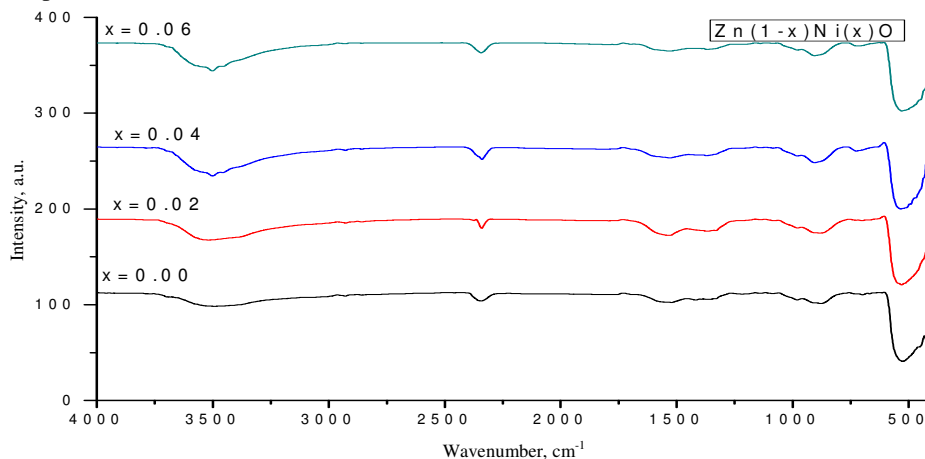


Figure 3. FTIR spectra of $\text{Zn}_{1-x}\text{Ni}_x\text{O}$ (for $x = 0.0, 0.02, 0.04$ and 0.06) nanocomposites

UV-Vis Study

Figure 4 shows UV-Visible spectra of $\text{Zn}_{1-x}\text{Ni}_x\text{O}$ ($x = 0.0, 0.02, 0.04, 0.06$) nanocomposites annealed at 400°C . Pure ZnO sample shows absorption band edge at 360 nm and observed band edge shows a shift towards higher wavelength side for the nickel doped sample *i.e.*, at $320, 310$ and 250 nm . The blue shift of the band edge for the nickel doped sample clearly indicates that Ni^{2+} ions are incorporated into the ZnO lattice²⁹⁻³¹ which confirms the results of XRD and FTIR results. Optical band gap was evaluated using the equation:

$$(\alpha h\nu)^n = A(h\nu - E_g) \quad (11)$$

Where α =absorption coefficient, $h\nu$ =photon energy, A =constant relative to the material and $n=2$ for direct band gap material or $1/2$ for an indirect band gap material. According to the equation, the optical band gap for the absorption peak can be obtained by extrapolating the linear portion of the $(\alpha h\nu)^2$ vs. $h\nu$ curve to zero and the observed energy gaps are 3.4, 3.8, 4.0 and 4.9 eV. These indicate that band gap of ZnO material increases with doping concentration of Ni^{2+} ions. The increase in the band gap or blue shift can be explained by the Burstein effect. This is the phenomena that the Fermi level merges into the conduction band with the increase of carrier concentration.

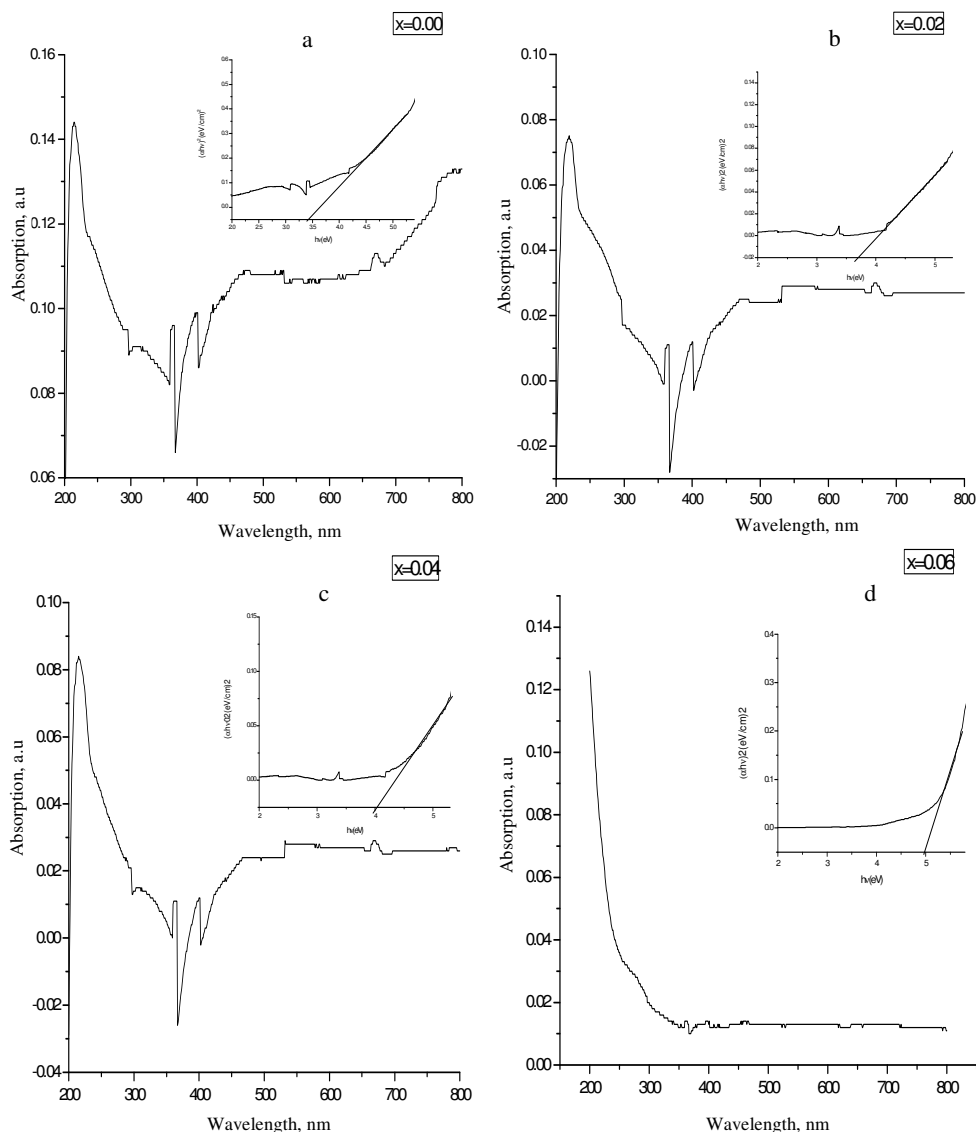


Figure 4. UV-Vis spectrum of $\text{Zn}_{1-x}\text{Ni}_x\text{O}$ (for $x = 0.0, 0.02, 0.04$ and 0.06) nanocomposites

TEM Analysis

TEM was employed to study the shape and size of nanocrystallites and to confirm the nanocrystalline structure of the prepared samples. Figure 5 shows the TEM images of nanocrystalline nature of undoped and doped ZnO samples. TEM images of undoped ZnO showed aggregates of non-uniform solids of different shape and size in the range 17-56 nm and nickel doped zinc oxide showed aggregates of smooth solids of nearly spherical shape in the range 15-43.0 nm. Different kinds of shapes like irregularly shaped nanoparticles, rectangular and hexagonally shaped nanoparticles are visible for the undoped nanoparticles. However, doped nanoparticles are of regular shapes, mostly spherical and its size is reduced with nickel doping which confirms the XRD results. The micrographs of the prepared samples reveal the compact arrangement of almost homogenous nanoparticles with nearly cubical and quasi spherical shape indicating crystalline nature of the metal. The particle size of the sample is decreased with increasing the concentration of nickel. The images clearly show the agglomeration of nanoparticles which may be attributed to the magnetic dipole interaction between the particles. The particle size determined from TEM is in agreement with XRD measurements. The histograms of the TEM images are shown in Figure 6.

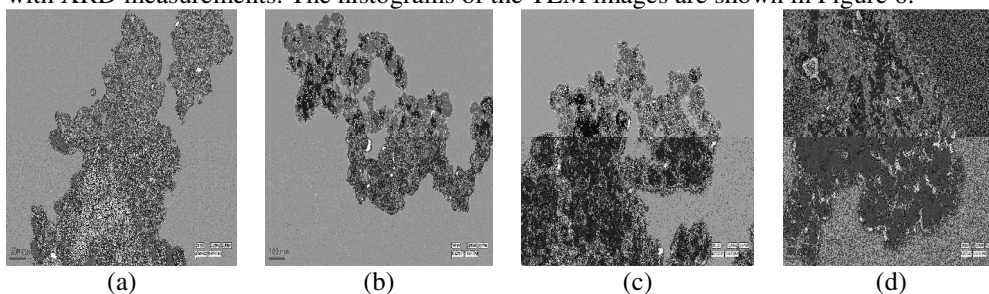
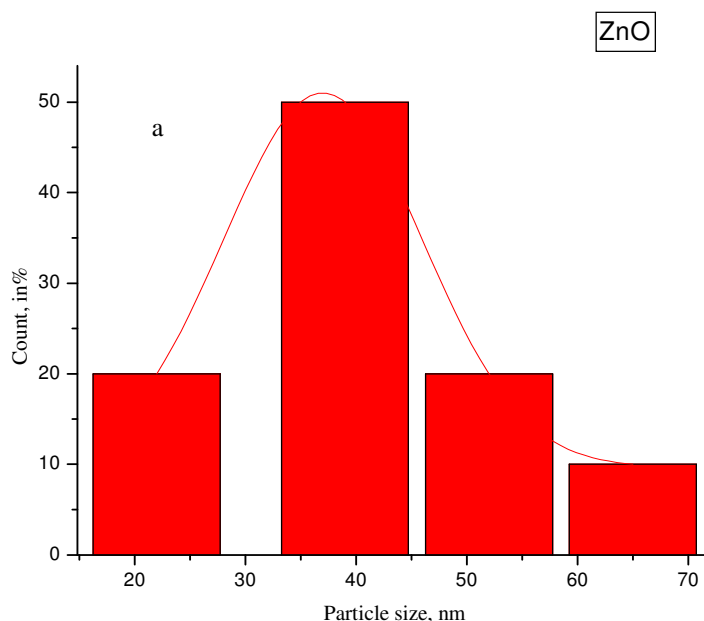
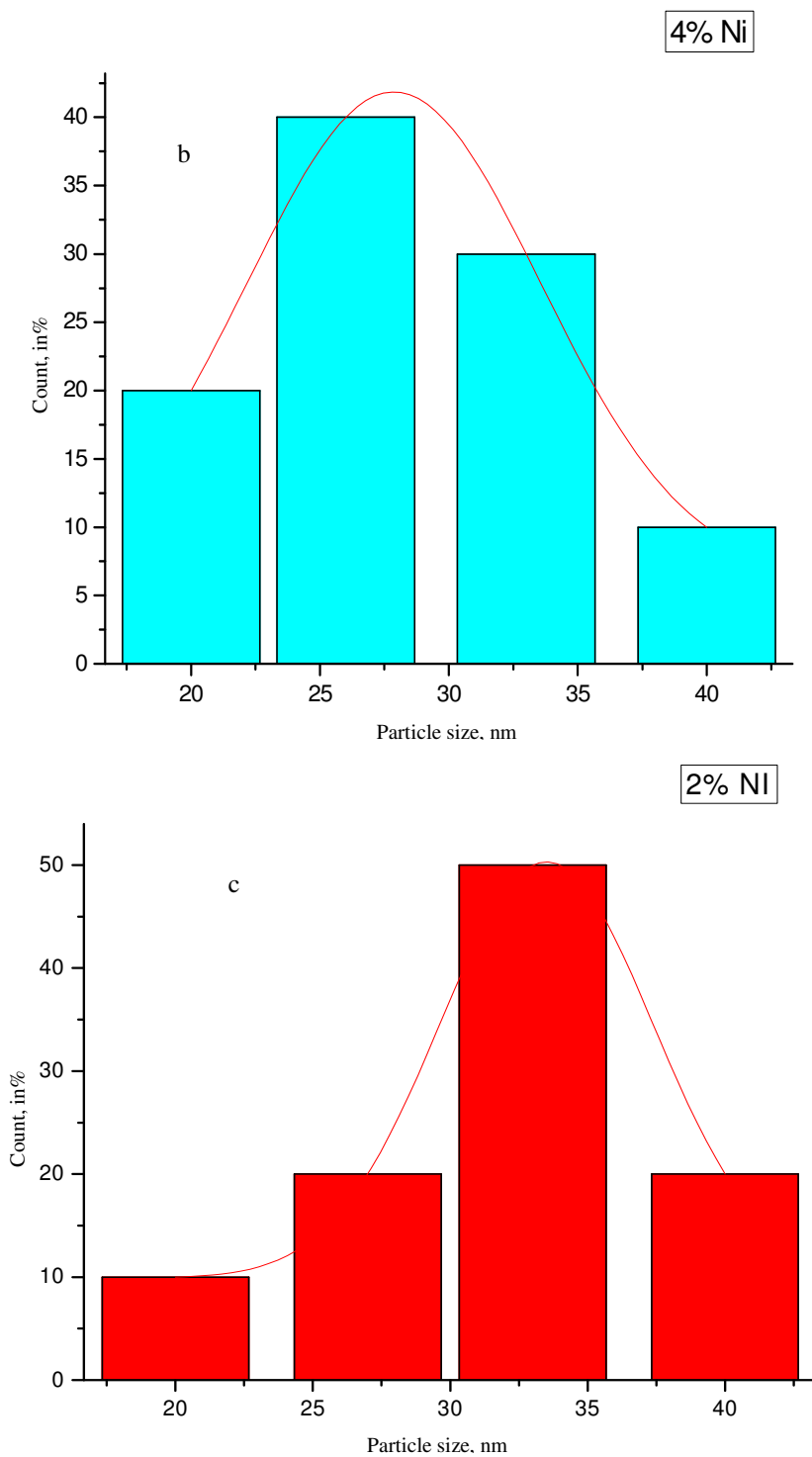


Figure 5. TEM microgram of $\text{Zn}_{1-x}\text{Ni}_x\text{O}$ (a) $x=0.0$, (b) $x=0.02$, (c) $x=0.04$, (d) $x=0.08$ nanocomposites





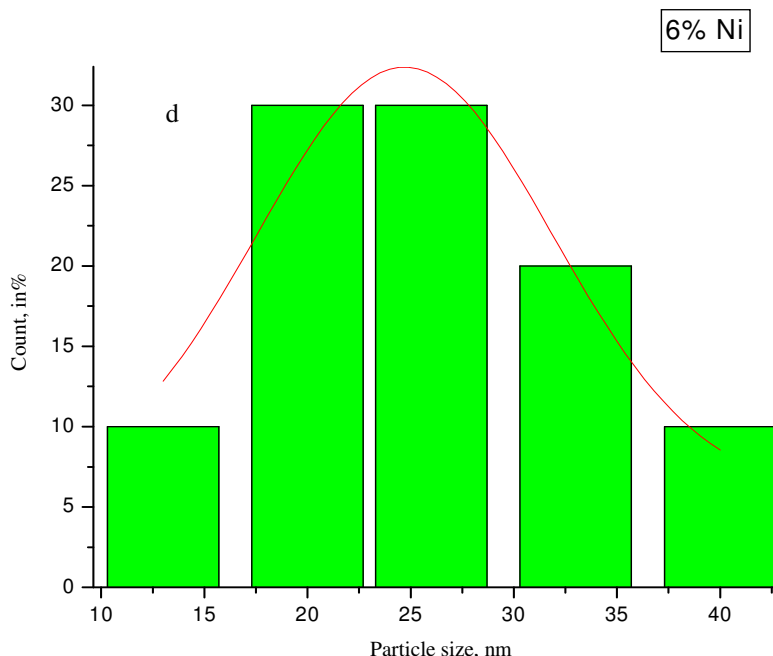


Figure 6. TEM Histogram of Zn_{1-x}Ni_xO (for x = 0.0, 0.02, 0.04 and 0.06) nanocomposites

Vibrating Sample Magnetometer (VSM) Study

Figure 7 shows the VSM results for Zn_{1-x}Ni_xO sample at room temperature. The bent natures of the curves clearly exhibits a shallow ferromagnetism in the samples. The paramagnetic component was subtracted from the original data in order to determine the ferromagnetic part. The value of magnetic resonance and coercivity of Zn_{1-x}Ni_xO samples are shown in Table 2. It can be observed that both coercivity and remanence increases with the addition of Ni in pure ZnO. Some ferromagnetic behavior observed in Ni doped ZnO, can be explained due to formation of nanoscale Ni-related secondary phase, such as Ni cluster or NiO. Firstly, the origin from NiO can be ruled out, as bulk NiO is antiferromagnetism at room temperature, secondly the existence of metallic Ni is also an unlikely source of this ferromagnetism because the synthesis of Ni-doped sample is performed in water as well as OH⁻ which can prevent the formation of metallic Ni nanocluster to some extent. Hence, ferromagnetism could be considered as a result of exchange interaction between free delocalized carriers and delocalized d spins in the Ni ions³²⁻³⁴. In order to study the magnetic behavior of pure and Ni doped ZnO nanoparticles as a function of magnetic field at room temperature, the M-H curve (Figure7) confirms that pure and Ni-doped ZnO nanoparticles show ferromagnetic ordering.

Table 2. Magnetic properties of Zn_{1-x}Ni_xO (for x = 0.0, 0.02 and 0.04) nanocomposites

x	Coercivity, Oe	Retentivity, emu/g	Saturation magnetization emu/g
0.00	185	0.057	0.10
0.02	226	0.050	0.12
0.04	97	0.064	0.18

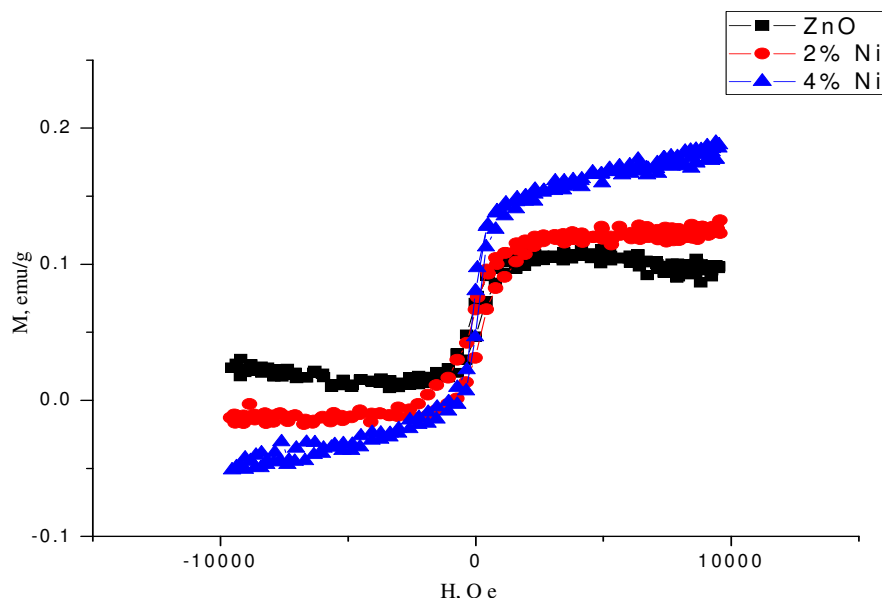


Figure 7. VSM Spectra of $\text{Zn}_{1-x}\text{Ni}_x\text{O}$ (for $x = 0.0, 0.02, 0.04$ and 0.06) nanocomposites

Conclusions

Nickel doped ZnO nanocomposites ($\text{Zn}_{1-x}\text{Ni}_x\text{O}$) have been prepared by co-precipitation method and changes in their structural, optical and magnetic properties as a function of doping concentration were investigated. The nanoparticles of Ni-doped ZnO continue to have a similar Wurtzite phase as that of undoped ZnO. The XRD pattern indicates that Ni-doping cause little or no structural disorder in the ZnO lattice, while the concentration of dopant was lower than 4%. With increasing Ni concentration, phase segregation takes place in the sample. The size of the nano particles and lattice constants decreases with increasing the dopant concentration due to mismatch of ionic radii. The FTIR analysis confirms the formation of defect centers in the structure and presence of functional groups and chemical bonding with Ni. The optical band gap of $\text{Zn}_{1-x}\text{Ni}_x\text{O}$ was calculated from the absorption spectra and it decreases with increase in nickel concentration. The observed red shift in the band edge of the nickel doped ZnO nanoparticles is due to the increasing sp-d exchange interactions between the band electrons and the localized d-electrons of the Ni^{2+} ions substituting Zn^{2+} ions in the doped sample indicating the substitution of Ni ion into the Zn site of the ZnO lattice. The morphology and microstructure of the samples were investigated by TEM which shows that nanoparticles are hexagonal and cubical in shape and the particle size estimated by statistical method is approximately 30, 24, 21 and 18 nm, respectively which were in accordance with the XRD results. Magnetic measurement studies reveals that all Ni- doped samples shows room temperature ferromagnetism which is attributed to oxygen/Zn vacancies and nickel dopant. The saturation magnetization increases and coercivity of the samples decreases well with increasing nickel doping.

References

1. Yang H M and Nie S, *Mater Chem Phys.*, 2009, **114**(1), 279-282; DOI:10.1016/j.matchemphys.2008.09.017

- 2 Saal H, Bredow T and Binnewies M, *Phys Chem Phys.*, 2009, **11**, 3201-3209; DOI:10.1039/B901596E
- 3 Zhung L J, Wu X M, Wu Z F, Yang X M, Chen X M and Chen Q, *Mater Chem Phys.*, 2010, **120(2-3)**, 480-483; DOI:10.1016/j.matchemphys.2009.11.036
- 4 Dinesha M L, Jayanna H S, Mohanty S and Ravi S, *J Alloys Compd.*, 2010, **490(1-2)**, 618-623; DOI:10.1016/j.jallcom.2009.10.120
- 5 Prinz G A, *Science*, 1998, **282**, 1660-1663; DOI:1126/science.282.5394.1660
- 6 Jaffe J E, Droubay T C and Chambers S A, *J Appl Phys.*, 2005, **97(7)**, 073908; DOI:10.1063/1.1868056
- 7 Prakash R, Song J I, Kumar S and Lee C G, *Int J Nanoscience*, 2011, **10**, 961-965; DOI:10.1142/S0219581X11008721 39
- 8 Wakano T, Fujimura N, Morinaga Y, Abe N, Ashida A and Ito T, *Physica E*, 2001, **10**, 260-264.
- 9 Yin Z, Chen N, Yang F, Song S, Chai C, Zhong J, Qian H and Ibrahim K, *Solid State Commun.*, 2005, **135(7)**, 430-433; DOI:10.1016/j.ssc.2005.05.024
- 10 Srinet G, Kumar R and Sajal V, *J Appl Phys.*, 2013, **114(3)**, 033912; DOI:10.1063/1.4813868
- 11 Liu X, Lin F, Sun L, Cheng W, Ma X and Shi W, *Appl Phys Lett.*, 2006, **88(6)**, 062508; DOI:10.1063/1.2170420
- 12 Satyarthi P, Ghosh S, Pandey B, Kumar P, Chen C L, Dong C L, Pong W F, Kanji Lal D, Asokan K and Srivastava P, *J Appl Phys.*, 2013, **113(18)**, 183708; DOI:10.1063/1.4804253
- 13 Singhal R K, Sharma S C, Kumari P, Kumar S, Xing Y T, Deshpande U P, Shripathi T and Saitovitch E, *J Appl Phys.*, 2011, **109**, 063907.
- 14 Kumar H, Dharam Veer and Dixit R M, *Chem Sci Trans.*, 2018, **7(1)**, 95-100; DOI:10.7598/cst2018.1462
- 15 Kumar H and Manisha, *Asian J Chem.*, 2018, **30(1)**, 59-62; DOI:10.14233/ajchem.2018.20853
- 16 Kumar H, Dixit R M and Dharam Veer, *Asian J Chem.*, 2017, **29(11)**, 1-5.
- 17 Kumar H and Manisha, *Asian J Pharma Clin Res.*, 2017, **10(9)**, 206-209; DOI:10.22159/ajpcr.2017.v10i9.19459
- 18 Li B B, Xiu X Q, Zhang R, Tao Z K, Chen L, Xie Z L, Zheng Y D and Xie Z, *Mater Sci Semicond Process*, 2006, **9(1-3)**, 141-145; DOI:10.1016/j.mssp.2006.01.074
- 19 Zhao Jing, Wang Li, Yan Xiaoqin, Yang Ya, Lei Yang, Zhou Jing, Huang Yunhua, Yousong Gu and Zhang Y, *Mat Res Bull.*, 2011, **46(8)**, 1207-1210; DOI:10.1016/j.materresbull.2011.04.008
- 20 Xingyu M, Wei Z and Youwei D, *J Magn Mater.*, 2008, **320**, 1102; DOI:10.1016/j.jmmm.2007.10.022
- 21 Lupana O, Chowla L, Chaic G, Roldana B, Naitabdia A, Schulte A and Heinrich H, *Mater Sci Eng B.*, 2007, **145(1-3)**, 57-66; DOI:10.1016/j.mseb.2007.10.004
- 22 Yu W, Yang L H, Teng X Y, Zhang J C, Zhang L and Fu G S, *Appl Phys.*, 2008, **103**, 093901; DOI:10.1063/1.2903524
- 23 Suryanarayana C, Norton M G X-ray Diffraction: a Practical Approach. Plenum Press Publishing, New York, 1998.
- 24 Biju V, Sugathan N, Vrinda V and Salini S L, *J Mater Sci.*, 2008, **43**, 1175-1179; DOI:10.1007/s10853-007-2300-8
- 25 Pandiyarajan T, Karthikeyan B, *J Nanopart Res.*, 2012, **14**, 647; DOI:10.1007/s11051-011-0647-x

-
- 26 Perales-Perez O, Parra-Palomino A, Singhal R, Voyles P M, Zhu Y, Jia W and Tomar M S, *Nanotechnology*, 2007, **18(31)**, 315606; DOI:10.1088/0957-4484/18/31/315606
- 27 Elilarassi R and Chandrasekaran G, *Optoelectronics Lett.*, 2010, **6(1)**, 6-10; DOI:10.1007/s11801-010-9236-y
- 28 Deka S and Joy P A, *Chem Mater.*, 2005, **17(26)**, 6507-6510; DOI:10.1021/cm051931i
- 29 Kim K J and Park Y R, *Appl Phys Lett.*, 2002, **81**, 1420; DOI:10.1063/1.1501765
- 30 Samanta K, Dussan S, Katiyar R S and Bhattacharya P, *Appl Phys Lett.*, 2007, **90**, 261903; DOI:10.1063/1.2751593
- 31 Weaklim H A, *J Chem Phys.*, 1962, **36(8)**, 2117; DOI:10.1063/1.1732840
- 32 Dianwu W, Mei Y, Zhongbing H, Guangfu Y, Xiaoming L, Yunqing K, Xianfu C and Hui W, *J Colloid Interface Sci.*, 2009, **330(2)**, 380-385; DOI:10.1016/j.jcis.2008.-10.067
- 33 Koseoglu Y, Durmaz Y C and Yilgin R, *Ceramics Internat.*, 2014, **40(7)**, 10685-10691; DOI:10.1016/j.ceramint.2014.03.053
- 34 Radovanovic P V and Gamelin D R, *Phys Rev Lett.*, 2003, **91**, 157202; DOI:10.1103/PhysRevLett.91.157202